PAPER

Check for updates

Exploring separation techniques for the direct recycling of high voltage spinel LNMO scrap electrodes†

Stiven López Guzmán, [ab] Marcus Fehse, *[a] Emanuele Gucciardi,[a]
Marta Cabello,[a] Silvia Martin,[a] Naiara Etxebarria,[a] Miguel Ceja,[a] Miriam Romera,[a]
Montse Galceran *[a] and Marine Reynaud *[a]

Among various recycling methods, direct recycling has emerged as a promising approach for recovering battery materials and directly reusing them to reduce carbon emissions and enhance the sustainability of the battery production process. Our study unveils, for the first time, different separation techniques for the delamination and the efficient direct recycling of high-voltage spinel $LiNi_{0.5}Mn_{1.5}O_4$ (LNMO) cathode materials from scrap electrodes, evaluating chemical, mechanical, and thermal separation techniques. The impact of the separation technique on the active material and the influence of the particle morphology and binder type (aqueous and organic solvent) on the outcomes of these separation techniques is assessed in terms of recovery yield, purity, and electrochemical performance. The recovered materials' physicochemical properties show minimal alterations after the recycling process. The investigated separation techniques allow the complete delamination of the electrodes and the recovery of around 90% of the active material. The recovered LNMO is used without further treatment for preparing new electrodes, which achieve 95% of the cycling capacity of pristine LNMO after 100 charge/discharge cycles. These lab-scale findings are validated on pre-pilot-line and commercial production-line-processed electrode scraps.

1 Introduction

Lithium-ion batteries (LIBs) are crucial for electronic devices and the energy transition, especially in the mobility sector. Hence, an exponential ramp-up in LIB production is expected in the upcoming years. This trend must be accompanied by an effort to establish a more sustainable battery production. A joint endeavor between manufacturers, researchers, and policy-makers is needed, focusing on the development of regulations (*e.g.*, EU battery regulation) and cell standardization methods, aiming to reduce greenhouse gas emissions, energy consumption and securing critical raw material supply, as recently summarized in different strategy documents.[1–4]

Geopolitical concerns, shortcomings, and price fluctuations can pose risks to critical raw materials, affecting the battery supply.[5] As a result, alternatives like recycling become

increasingly crucial for sourcing battery materials, thereby providing a more sustainable option compared to the traditional mining of virgin materials.[6–9] The ramping up of battery production will consequently lead to a greater volume of materials to be recycled during both the battery production stage (*i.e.* battery scrap) and later at the end of life (EOL),[10,11] as depicted in Fig. 1.

Today, there are three main ways of recycling batteries: pyrometallurgy, hydrometallurgy, and direct recycling.[12] Their positioning within the general battery life-cycle is depicted in Fig. 1. Pyrometallurgy recycling uses high temperatures to melt the metallic elements and burn the non-metallic content, allowing only the recovery of selected metal alloys and ores.[13] Hydrometallurgical recycling involves three main steps: leaching spent cathode material, removing impurities/purifying the leach solution, and recovering the transition metal and lithium salts.[14] The resulting ores and salts from both processes can be used to synthesize new battery materials (closed-loop recycling) or other applications (open-loop recycling). However, these closed-loop processes require the re-synthesis of the active material, increasing their energy requirement and resource footprint.[15]

Direct recycling involves recovering different battery components without altering their chemical or physical properties, allowing their direct reintroduction into new cells or

[a]Center for Cooperative Research on Alternative Energies (CIC energiGUNE), Basque Research and Technology Alliance (BRTA), Alava Technology Park, Albert Einstein 48, Vitoria-Gasteiz, 01510, Spain. E-mail: mfehse@cicenergigune.com; mgalceran@cicenergigune.com; mreynaud@cicenergigune.com

[b]Chemical and Environmental Engineering Department, Faculty of Science and Technology, University of the Basque Country, UPV/EHU,B Sarriena s/n, Leioa, 48940, Spain

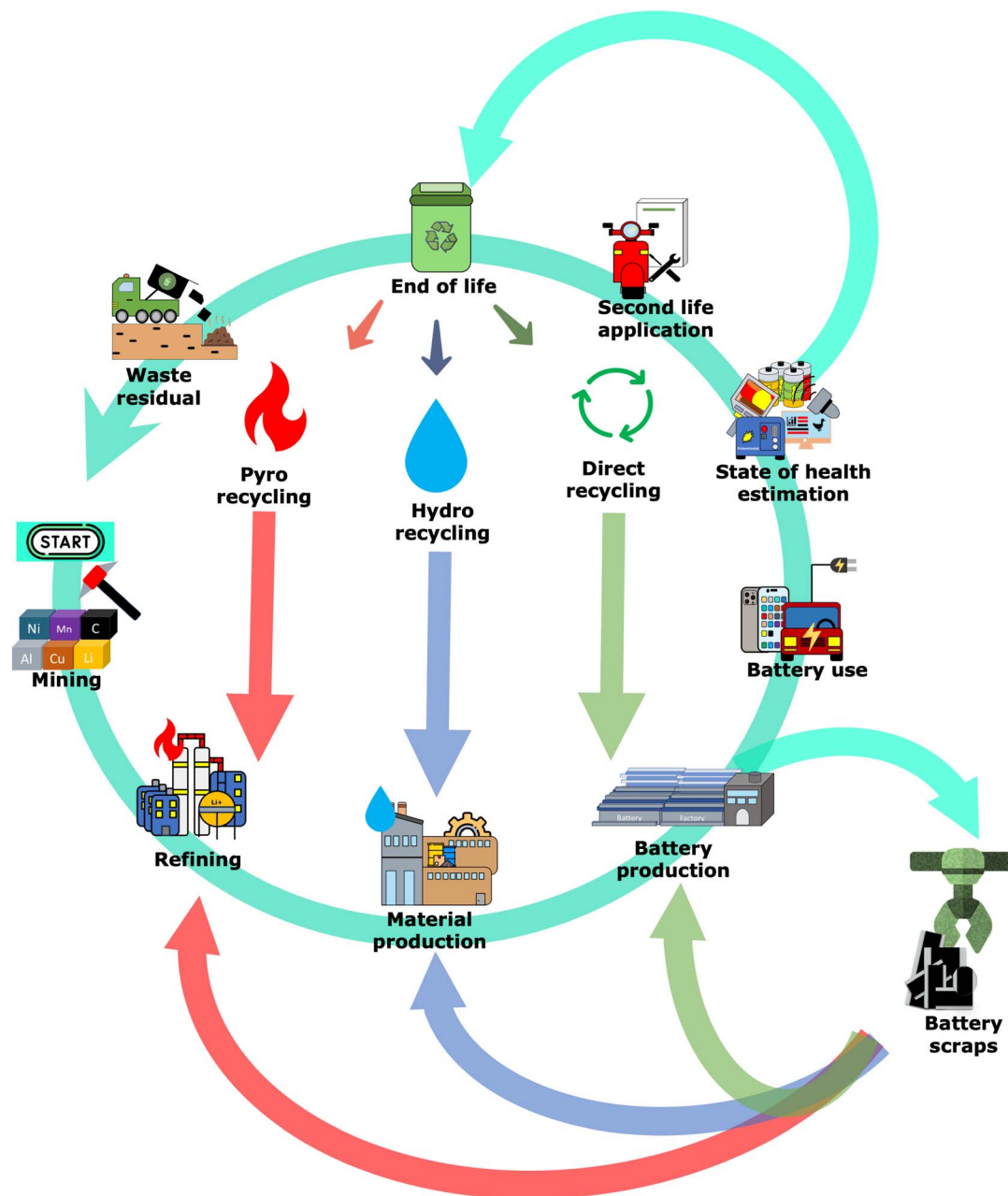† Electronic supplementary information (ESI) available. See DOI: https://doi.org/10.1039/d4ta07642g

2690 | *J. Mater. Chem. A*, 2025, **13**, 2690–2706

This journal is © The Royal Society of Chemistry 2025

Fig. 1 Lithium-ion battery life cycle and the principal recycling routes depicting the origin of two main sources of recyclable materials; *i.e.* from end-of-life batteries (top) and from battery production scraps (bottom).

blending with pristine material without further treatment of the material.[16–18] As a result, this approach is significantly more resource- and cost-efficient than the traditional pyro- and hydrometallurgical recycling methods,[19,20] offering, in particular, a viable recycling option for materials that do not contain high-value metals, such as $LiFePO_4$ (LFP) or anodes.[21,22] Another advantage of this technique is that it allows the recovery of the metallic current collector, which can be recycled for other applications or directly reused for LIBs after further processing.[23]

In contrast to traditional recycling methods, direct battery recycling has yet to achieve commercial maturity despite its

attractive assets. This backlog can be attributed to various limitations, like the need for manual disassembly of the cells, the challenging sorting and delamination of the active materials, the development of regeneration technologies for spend materials, and their respective scale-up to an industrially relevant scale.[24–26] These aspects must be addressed in future battery cell designs to allow more straightforward and efficient direct recycling.[27,28]

Due to the different requirements in the battery sector, manufacturers and researchers are investigating different streams of materials to recycle, from spent batteries to in-house manufactured residuals (battery scraps). As of today, battery

scraps are the most abundant and accessible source of battery material for recycling. According to recent studies, these battery scraps are projected to dominate the recycling market, accounting for over 50% of the materials to recycle and remaining the primary source until 2030.[29,30] As more batteries reach the end of their lifetime (EoL), the dominance of scrap will gradually decrease in importance as a greater number of EoL batteries enter the recycling stream.

Scrap electrodes consist of battery materials that are not assembled into a functional battery. These materials are typically deemed unusable for various reasons, including trimming from production, out-of-specification materials, assembly errors, in-development materials, *etc.*[31] Currently, these scraps, also known as prompt scrap or pre-consumer scrap, dominate the market and are deemed to retain considerable value, and their direct reuse seems more viable than other types that come from end-of-life products.[32]

A critical step in the direct battery recycling of scrap electrodes involves devising efficient methods for delaminating and recovering the active material without compromising its properties.[33,34] These methods can be broadly classified into three categories: (i) chemical separation technique, which utilizes solvents to separate active materials; (ii) mechanical separation technique, which relies on the application of an external force to break the binder bonds of the cathode active material (CAM) with the metallic collector; and (iii) thermal separation technique, which uses temperature in order to decompose specific components of the electrode aiming to facilitate the delamination.

The chemical separation technique relies on a principle called competitive inhibition of the hydrogen bonding between the cast electrode and the surface of the current collector. It works by interrupting the chemical pathway of one substance to enter and compete for the binding ability.[35] This entails the separation of the cast electrode in the presence of a suitable solvent, based on its Hansen solubility parameter, to remove the binder.[36] While dipolar solvents like 1-methyl-2-pyrrolidone (NMP) can dissolve binders such as Polyvinylidene Fluoride (PVDF),[37] resulting in the effective direct recycling of the battery materials,[38] cost, health, and environmental concerns of using NMP make it necessary to search for alternatives. In this regard, Cyrene™ has shown to be a suitable candidate, with several works showcasing efficient removal of $LiNi_{1-x-y}Mn_xCo_yO_2$ (NMC) cathode material while at the same time being more cost-efficient and benign than NMP. For instance, Bai *et al.* reported the recovery of NMC, which shows a capacity of 158 mA h g^{-1}, maintaining almost 93% of the pristine capacity after 40 cycles.[35,39]

Different routes for the mechanical separation technique have been explored for electrode separation, including ultrasonic waves, manual peeling, centrifugation, or froth flotation.[40–42] In the case of using ultrasonic waves, the working principle consists of pulsating shock waves applied to the material's surface through a liquid medium. The acoustic stimulation triggers a reaction through cavitation of bubbles induced by ultrasonic waves.[40] These bubbles, subjected to intense vibration, burst at high energy, thereby generating

potent shockwaves that cause delamination.[43] Unfortunately, most of these works are limited to process descriptions and do not provide material characterization or electrochemical benchmarks for recycled material. An exception is the work of X. Chen *et al.*, which, using ultrasound and a chemical reagent, managed to recover LFP effectively from spent batteries. Their results indicate an improvement in the capacity of the recycled LFP (160 mA h g^{-1}, maintaining a capacity retention of 91% after 200 cycles) in comparison with the spent LFP (152 mA h g^{-1}) but lower compared to the pristine LFP (167 mA h g^{-1}).[42]

Another approach is the thermal separation technique, which provides a direct and scalable path for active material separation. This process aims to remove the binder and the conductive carbon by surpassing their thermal decomposition temperature while preserving the structure of the active material.[17,44] This method has been explored in spent cells for diverse chemistries such as $LiMn_2O_4$ (LMO), $LiCoO_2$ (LCO), and NMC. In the vast majority of today's cathode electrodes, the binder to remove is PVDF. The principal concern when working with PVDF-based electrodes is the release of hazarous HF during thermal treatment, which can be controlled by using a solvent trap in the furnace's exhaust. In the work of Zhang *et al.*, the directly calcined NMC cathodes (600 °C) achieved a discharge capacity of 121 mA h g^{-1} after 200 cycles at 1C, with a capacity retention of almost 91%.[45] Other authors report the use of low temperature of 250 °C to allow the peeling off of the CAM from the current collector by hand scraping.[46] In another work, Giles *et al.* proposed a two-step thermal treatment process (450–500 °C and 800–850 °C) in a furnace with extraction, adding extra LiOH to recover the lithium deficiency of the initial material and reporting a comparable initial discharge capacity for NMC532 materials of 164 mA h g^{-1}.[47]

Despite the widespread use of the LIB, cell chemistry like NMC raises certain concerns regarding the safety and sourcing of the components (Co) used for fabrication. Co-free spinels CAM has gained much attention in the effort to produce cheaper and less critical raw materials for the intensive production of cathode materials. Among them, the spinel material $LiNi_{0.5}Mn_{1.5}O_4$ (LNMO) is a promising candidate for next-generation of LiBs, thanks to features like its fast Li-ion exchange, high thermal stability, and increased structural and chemical stability, which enable cost-efficient and environmentally benign aqueous electrode processing.[48–50] Depending on the synthesis conditions, it is possible to obtain the crystallized cubic phase, which can be either a transition metal (TM) ordered phase ($P4_332$) or a TM disordered phase with increased symmetry ($Fd\bar{3}m$).[51]

Notwithstanding its widespread research exploration, LNMO cathode chemistry continues to face challenges that have delayed its implementation, such as stabilizing the SEI, finding stable electrolytes, and suppressing the TM dissolution during cycling.[52,53] Despite these remaining challenges, LNMO's commercialization seems to be within reach according to recent announcements.[54,55] However, as of today, no study has investigated the possibility of recycling it. Therefore, it is essential to start considering the different scenarios for the recycling of

2692 | *J. Mater. Chem. A*, 2025, **13**, 2690–2706

This journal is © The Royal Society of Chemistry 2025

LNMO to adopt novel tendencies like design for recycling or circular economy process in pursuit of an increase in its competitiveness and sustainability.

In this study, we aim to investigate, for the first time to the authors' knowledge, the feasibility of direct recycling of LNMO scrap materials in light of its potential mass-scale commercialization. The principal objective is to evaluate the impact of particle type and binder type of different LNMO electrodes by three different separation techniques for direct recycling, thereby avoiding resource-intensive re-synthesis. The recovered materials are thoroughly analyzed to assess any physical and electrochemical properties alterations. Furthermore, the proposed separation techniques are benchmarked in terms of the recovered material's purity, convenience, energy consumption, and other key indicators.

2 Materials and methods

2.1 Electrode preparation

2.1.1 Electrodes prepared from virgin materials. LNMO scrap electrodes were obtained from the pre-pilot line at CIC energiGUNE, as well as from two distinct industrial pilot lines at SAFT batteries and the Austrian Institute of Technology (AIT). The electrodes were fabricated using two distinct types of spinel LMNO as CAM with spherical particle shape (LNMO-S) and polygonal particle shape (LNMO-P) supplied by TOPSOE. The electrode production used two different binders, Polyvinylidene fluoride (PVDF) or carboxymethyl cellulose (CMC) + latex, used for organic and aqueous electrode processing, respectively. The electrodes will be denoted as Pristine-S or Pristine-P, depending on the type of LNMO employed for the fabrication.

At the pre-pilot line, for the organic solvent electrode processing, the CAM was mixed with the binder PVDF (Kynar® HSV 900, Arkema) and the conductive additive C65 (TIMCAL C-NERGY™ SUPER C65, Imerys) in 1-methyl-2-pyrrolidinone (NMP, Sigma Aldrich). The formulation consisted of 93 wt% LNMO, 4 wt% C65 and 3 wt% PVDF. The materials were mixed in a dissolver (Dispermat®CV3-PLUS) for a total processing time of 5 hours and a maximum speed of 800 rpm. The resulting slurry was cast onto a carbon-coated aluminum foil (Armor) and vacuum dried at 80 °C for 2 hours. Afterward, the electrodes were calendered at 80 °C with a speed of 0.5 m min^{-1}. This resulted in electrodes with around 2 mA h cm^{-2} loadings of both LNMO types in a single-side carbon-coated aluminum foil of around 24 cm × 12 cm.

For aqueous-based electrode processing, C65 was replaced by C45 (TIMCAL C-NERGY™ SUPER C45, Imerys), and a mixture of Latex (Kynar® Latex 32, Arkema) and CMC (Wallocel) solution (3 wt%) was used as binders. The total mixing time was 6 hours at a maximum speed of 1500 rpm. Then, the slurry was cast onto a carbon-coated aluminum current collector and consequently dried at 80 °C for two hours. Subsequently, the resulting electrodes underwent calendering at 80 °C with a speed of 0.5 m min^{-1}. The obtained electrodes present loadings of ≈2 mA h cm^{-2} of both LNMO types deposited in single-side carbon-coated aluminum foil of around 24 × 12 cm.

The electrodes made and calendered in the pilot facilities by SAFT and AIT share similar formulations, with loadings of around 2–2.5 mA h cm^{-2}. The SAFT electrode scraps were 17 cm × 8 cm on double-coated aluminum. The AIT electrode scraps were around 24 cm × 10 cm on single-coated aluminum. The electrode laminates produced by AIT and SAFT were prepared exclusively via aqueous processing using the LNMO-S type CAM.

Finally, for electrochemical testing, disks were cut from the resulting electrode sheets, using a 12 mm handheld puncher from Nogamiken Co, left to dry in a vacuum oven (Büchi) at 120 °C for 16 h to eliminate moisture and humidity before being introduced into a glovebox with an inert argon atmosphere.

2.1.2 Electrodes made from recovered CAM. Once the separation was achieved (see below), the materials recovered from the different separation methods (chemical, mechanical, and thermal techniques) were directly used to fabricate new electrodes without further treatment, see Fig. 2(a). The formulation used consisted of 90 wt% cathode active material (LNMO), 5 wt% conductive agents (C65, Imerys), and 5 wt% of polymeric agglutinant (1% CMC-Wallocel and 4% latex-Kynar® Latex 32), all dispersed in water using an Ika ultra-turrax T25 digital stirrer (IKA-Werke GmbH). The total processing time was 2 hours at 16 000 rpm. The slurry was cast onto aluminum foil using a doctor blade with a 0.25 mm thickness and subsequently dried overnight in a vacuum oven at 80 °C. Lastly, electrodes were punched with a 12 mm handle electrode puncher, then pressed at 2 tons for 30 seconds and dried in a Büchi vacuum oven at 120 °C to be inserted in the glovebox for cell assembly. The resulting electrodes present loadings around 1 mA h cm^{-2}.

2.2 Separation methodologies

2.2.1 Chemical separation. Cyrene solvent was heated to 105 °C in a round bottom flask with a multi-neck connected to a cooling column. The scrap electrodes were cut into small pieces of 2 cm × 2 cm and then immersed in the heated liquid for an hour while constantly stirring, triggering the delamination of the electrodes. While still hot, the mixture of the heated Cyrene and the delaminated cathodes was placed into centrifugation tubes, and the current collector pieces were set aside. The mixture was then centrifuged for thirty minutes at 12 000 rpm, allowing the separation between the CAM powder, the solvent and the other components (i.e. carbon, PVDF, and Al). After the initial centrifugation, the liquid component containing Cyrene, PVDF, and carbon can be separated by decantation. Additional centrifugation of the solid wet powder with distilled water was performed to allow the separation of the conductive carbon from the CAM and remove the remnants of Cyrene by centrifugation of the sample twice, using the same conditions as above. The resulting powder was dried overnight in a vacuum oven to remove any remaining water. It should be noted that it is possible to recuperate both the solvent and polymeric binder by employing a thermally induced phase separation process (TIPS); furthermore, the separated Cyrene can be reused, as previously reported by Y. Bai et al.[39]

This journal is © The Royal Society of Chemistry 2025

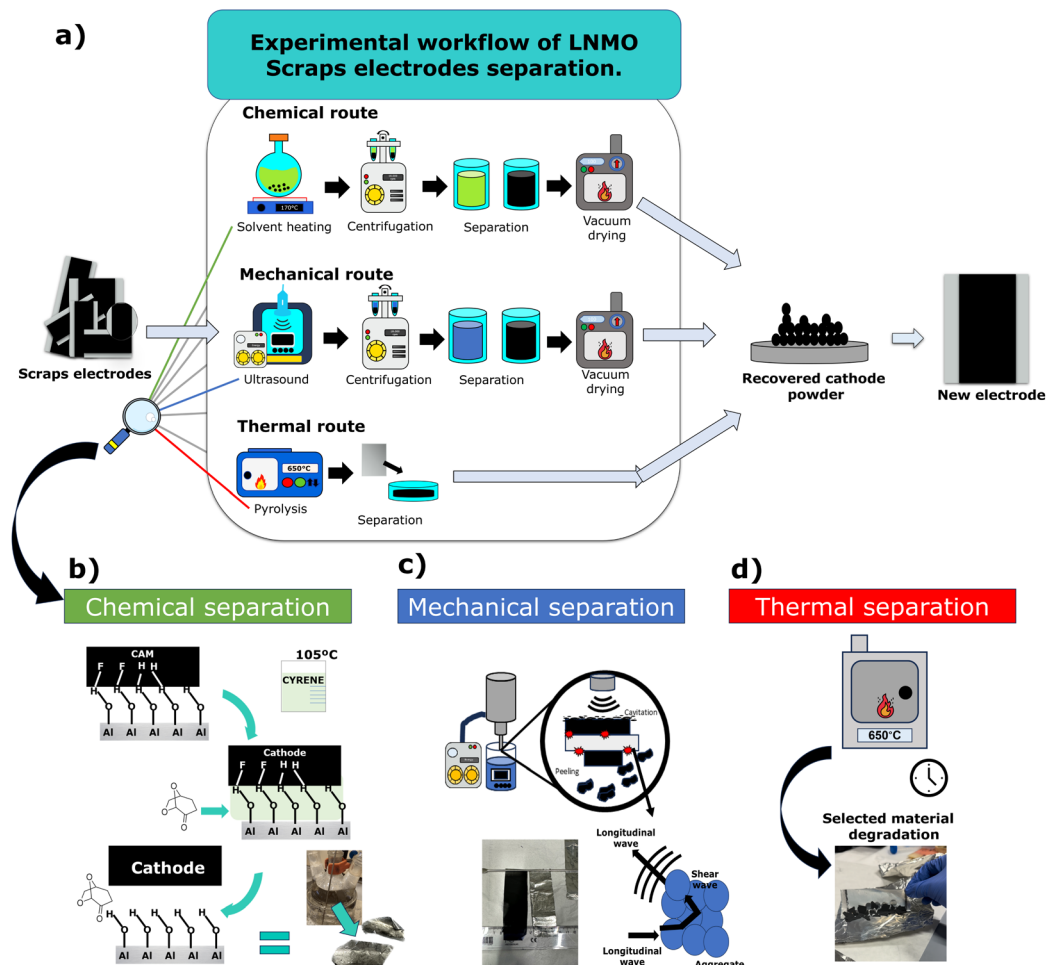J. Mater. Chem. A, 2025, 13, 2690–2706 | 2693

Fig. 2 (a) Graphical description of the recycling process for scrap electrodes utilizing different separation routes. The bottom part includes a detailed schematic of the separation mechanisms for (b) chemical separation using heated chemical reagents, (c) mechanical separation using ultrasound waves, and (d) thermal separation through temperature treatment.

2.2.2 Mechanical separation. CMC-based LNMO cathode electrode scraps were immersed in distilled water and treated with ultrasound using a Branson Sonifier 250 with a 1/8 tapered microtip, capable of delivering a maximum output of 250 W at a frequency of 20 kHz. A continuous wave was applied for two minutes at 20% of the system's total energy. The physical force of the ultrasonic machine facilitates the separation, resulting in the electrode's delamination. The mixture was then subjected to three stages of centrifugation, each lasting thirty minutes at 12 000 rpm. The supernatant, which contained most of the carbon due to its hydrophobic nature, was discarded, and the remaining wet powder was collected and dried overnight to eliminate any remaining moisture.

2.2.3 Thermal separation. For the thermal separation, the CMC-based electrode scraps were subjected to a calcination process. For this, the LNMO electrodes were gradually heated in air at a rate of 5 °C min^{-1} until reaching 650 °C, followed by one hour of annealing. The CAM was removed by gently moving the current collector, which can also be recovered. No additional purification steps were undertaken.

2.3 Recovery rate and purity estimation

The recovery rate (RR) determines how much cast electrode materials were retrieved from the scrap electrodes. It is calculated from the amount of recovered material powders ($M_{recovered}$) with respect to the mass of the scrap electrodes (M_{scrap}) minus the mass of the carbon-coated aluminum current collector (M_{CC-Al}), as indicated in eqn (1).

$$\text{RR} = \frac{M_{recovered}}{M_{scrap} - M_{CC-Al}} \times 100\% \quad (1)$$

The purity evaluates how much of the desired CAM is contained in the overall recovered material powders. The relative residual content was obtained by elemental analysis and ICP, where the former estimates the content of organic residuals (*e.g.* carbon), and the latter aims to assess the inorganic metals (iron, aluminum). To enhance statistical reliability, the separation trials were repeated four times. The individual RR and purity percentages were used to calculate the process's average value and standard deviation.

2694 | *J. Mater. Chem. A*, 2025, **13**, 2690–2706

This journal is © The Royal Society of Chemistry 2025

2.4 Materials and electrode characterization

The X-ray diffraction (XRD) patterns of the pristine and recovered materials were acquired using a Bruker D8 Discover X-ray diffractometer equipped with a LYNXEYE XE detector with the Cu K$_\alpha$ radiation ($\lambda = 1.54060$ Å) in the 2θ range 10°–80°. Le Bail fits of the XRD patterns were carried out using the FullProf Suite software[56] to determine the unit cell parameters of the LNMO phase for each sample.

Micrographs were taken on a Thermo Fisher Quanta 200 FEG high-resolution Scanning Electron Microscope (SEM) with a working voltage of 10 kV. The average particle size was calculated with the Image J software, measuring an average of 30 particles.

The particle size distribution of the recovered powders was evaluated with a MasterSizer 3000 (Malvern Panalytical, Netherlands), using distilled water as a dispersant. A refraction index of 1.54 and an absorption index of 0.01 were used for the measurement parameters, and a nonspherical particle mode was assumed in the model. The samples were measured twice in six iterations to ensure good reproducibility.

Elemental analysis was done twice on each sample using a ThermoFlash 2000 organic elemental analysis under a argon atmosphere at 800 °C, to measure organic residuals (C, H, N, S).

The Raman spectra were recorded with a Renishaw spectrometer (Nanonics Multiview 2000) operating with an excitation wavelength of 532 nm. Spectra were acquired with 15 s of exposition time of the laser beam to the sample in three different spots to ensure reproducibility.

The thermogravimetric analysis (TGA) allowed the study of the scrap electrodes' thermal stability and decomposition behavior. The test was conducted in a Netzsch TG 209 F1, with a 5 °C min^{-1} heating speed from 30 °C to 800 °C under an argon atmosphere. The objective was to determine the different degradation temperatures of the materials under different temperature ranges.

The analysis of the composition of the recovered powder samples was done with inductively coupled plasma-atomic emission spectroscopy (ICP-AES) using a Horiba Ultima 2 (Jobin Yvon, Longjumeau, France) in conjunction with an AS500 autosampler and Activanalyst software (version 5.4). The ICP-AES operating conditions were as follows: 1.1 kW of RF power, 11.8 L min^{-1} of a plasma-gas flow rate, 0.2 L min^{-1} of a sheath-gas flow rate, and 0.02 L min^{-1} of a nebulizer-gas flow rate. Solutions were introduced into the plasma torch using a nebulizer and a cyclonic spray chamber at a flow rate of 0.85 mL min^{-1}. The wavelengths (nm) employed in the ICP-OES analysis are 396.152 nm for aluminum, 670.784 nm for lithium, 260.569 nm for manganese, and 221.647 nm for nickel determination.

Li Magic Angle Spinning solid-state Nuclear Magnetic Resonance (MAS NMR) experiments were performed on a Bruker 300WB spectrometer charged to a field of 4.69 T equipped with a standard 1.3 mm MAS probe. Spinning frequencies were set to 50 kHz. A rotor-synchronized spin-echo pulse sequence was used with typical 90° and 180° pulses of 1.3 and 2.6 μs, respectively. A recycle delay of 0.7 s and 2 s was used, and around 89 k and 1 k scans were typically acquired in a ^{6}Li and ^{7}Li NMR experiment, respectively. The recycle delays were set to ensure complete relaxation of the spins. The spectra were referenced to a 1 M solution of LiCl (set at 0 ppm). The spectra were analyzed and deconvoluted using the Dmfit software package.

The peel-off tests of the electrodes were performed using an Instron 34SC-5 universal machine at 90° with four repetitions of 7 cm long electrode strips, and standard tape to obtain an average value.

2.5 Electrochemical testing

The positive electrodes were mounted in CR2032 coin cells (MTI), using a 12 mm lithium disk as a counter electrode and a 14 mm diameter glass fiber separator (Whatman GF/D). The separator is impregnated with 100 μL of LP30 (lithium hexafluorophosphate in (1 : 1 vol%) ethylene carbonate : dimethyl carbonate) electrolyte. The coin cells were sealed using a crimping machine at a pressure of 500 psi (kg cm^{-2}) for 30 seconds. The electrodes were electrochemically evaluated using a Neware cycler (BTS4000-5V & 6A). A cycling protocol (described in Table S1†) consisting of 9 steps and 100 cycles performed in a climatic chamber at 25 °C. Four initial formation cycles at constant current and constant voltage (CCCV), 15 power cycles, and 81 cycles were followed to measure capacity retention. The C-rate was calculated based on the LNMO's theoretical specific capacity of 147 mA h g^{-1}.

For the calculation of the Mn redox contribution to the capacity of the system, the 4V capacity is defined according to eqn (2), where $Q_{\text{cha}}^{\text{4V}}$ and $Q_{\text{dis}}^{\text{4V}}$ correspond to the capacity value achieved between the 3.5 to 4.3 V region during the charge and discharge, respectively. Meanwhile, the $Q_{\text{dis}}^{\text{tot}}$ corresponds to the capacity value between 3.5 and 4.9 V during the discharge.[57] The values are calculated from a measurement made at a cycling rate of 0.2C.

$$4 \text{ V capacity contribution} = \frac{Q_{\text{cha}}^{\text{4V}} + \left(Q_{\text{dis}}^{\text{tot}} - Q_{\text{dis}}^{\text{4V}}\right)}{2 \times Q_{\text{dis}}^{\text{tot}}} \quad (2)$$

In the same sense, it is also possible to determine the stoichiometric coefficient of both TMs based on their electrochemical capacity contribution using the eqn (3) and (4). The Ni-related stoichiometry is calculated by subtracting the 4 V capacity from the total capacity and dividing it by the total capacity. As each Ni releases two electrons upon oxidation, a factor two must be included. As the sum of the TM in the spinel structure has to be two, the Mn stoichiometry can be obtained by subtracting the computed value of Ni from the total ideal stoichiometric number.

$$v(\text{Ni}) = \frac{\left(Q_{\text{dis}}^{\text{tot}} - Q_{\text{dis}}^{\text{4V}}\right)}{2 \times Q_{\text{dis}}^{\text{tot}}} \quad (3)$$

$$v(\text{Mn}) = 2 - v(\text{Ni}) \quad (4)$$

2.6 Energy consumption estimation

The amount of energy needed for any heating processes used in this study was estimated based on eqn (5), where Q is the

This journal is © The Royal Society of Chemistry 2025

J. Mater. Chem. A, 2025, **13**, 2690–2706 | **2695**

amount of energy needed to heat a mass m with heat capacity c by ΔT degrees.

$$Q_{heat} = m \times c \times \Delta T \tag{5}$$

for the thermal treatment, a muffle oven of 18 kg (6 L capacity) lined with refractory material of $c = 900$ J kg^{-1} K^{-1} was used. The maximum temperature of 650 °C was held for 1 h assuming a heat dissipation of 200 W (P_{loss}); the heat loss was estimated using eqn (6)

$$Q_{loss} = P_{loss} \times t \tag{6}$$

The total energy required for the thermal separation is hence sum of energy required for the heating and dissipated energy, which add up to 10.73 MJ.

The energy input required for the chemical method comprises heating 0.15 L of aqueous Cyrene solution to 105 °C and maintaining it for 1 h. It can be calculated analogous to the above example assuming a heat capacity of $c = 4.19$ J kg^{-1} K^{-1} and a heat dissipation (P_{loss}) of 100 W. The resulting energy input for the chemical technique would be 0.4 MJ. Additionally, a drying step at 100 °C under air is carried out in a drying oven with 36 L capacity and 35 kg weight lined by stainless steel ($c = 490$ J kg^{-1} K^{-1}) and maintained for 16 h, heat loss estimated to 50 W (P_{loss}), would require 4.2 MJ. The heat needed to evaporate the water remnant is considered negligible. Hence, the total energy input is 4.6 MJ for the chemical separation technique.

For the mechanical separation, the energy input for sonication is assumed based on the power input described above 20% of 250 W during 120 s using eqn (6) resulting in 0.06 MJ. Additionally, the energy for the drying step must be considered, resulting in a total energy consumption of 4.26 MJ.

2.7 Convenience indicator estimation

To evaluate the practical aspects of the different separation techniques, such as ease of separation, number of processing steps required, and overall processing time needed, these categories were rated on a 1 to 10 scale. In contrast, higher points indicate faster and easier procedures. The points were summed up for each separation methodology, and the value of the highest-ranking technique finally normalized the total values.

3 Results

The LNMO cathode active material powders were recovered from four types of scrap electrodes (*i.e.*, Pristine-S and Pristine-P electrodes obtained from aqueous and organic solvent-based processing) employing three different separation methods: chemical, mechanical, and thermal techniques. A general resume of each process is presented in Fig. 2(a). The chemical and mechanical separation techniques involve four steps: delamination of the CAM, centrifugation of the solid/liquid mixture, removal of carbonaceous and binder residuals, and vacuum drying of the resulting recovered CAM powder. In the case of the thermal separation technique, only the electrode

delamination and manual recovery of the powder are required after heating the electrode scraps to collect the recovered CAM.

The LNMO-S powder CAM consists of spherical secondary particles with ≈ 10 μm diameter, while LNMO-P has polygonal-shaped particles with an average size of around 1 μm, as shown in Fig. 3(a) and (d). The electrodes prepared with this material allow easy processability and homogeneity; see SEM top view of the pristine electrodes Fig. 3(b) and (e) Both samples present similar compositions, with a slightly Ni-deficient stoichiometry with Ni to Li ratio of ≈ 0.45, as revealed by ICP-AES measurements (see Table S2†). Their respective XRD patterns are depicted in Fig. 3(c) and (d). The results of the Le Bail fit of these patterns using a single spinel phase (SG: $Fd\bar{3}m$) show that the samples have high purity. No trace of rock salt impurities or the presence of additional phases was detected. The refined lattice parameter of the spinel phase are 8.187(18) Å and 8.186(9) Å for Pristine-S and Pristine-P, respectively (Table S3†).

As an initial step, the separation conditions were evaluated. It was found that organic processed PVDF-based electrodes present significant drawbacks for their separation *via* the mechanical and thermal separation techniques due to the type of binder employed. In the case of the former, the challenge lies in the inability of the ultrasound to delaminate the CAM from the current collector due to the strong adhesion of PVDF binders. To overcome this, a degradation of the binder *via* a highly oxidative reagent (*e.g.*, Fenton reagent) combined with ultrasound is necessary, resulting in increased recycling costs and resources of the recycling process.[42] In the case of thermal separation, the drawback lies in the formation of hazardous by-products like hydrofluoric acid. Albeit the toxic gases can be captured with a solvent trap, working with this type of side product is complex and poses risks to human health.[45,58] Consequently, in this study only the the organic solvent processed electrodes were subjected to chemical separation.

Analogous to Cyrene for the removal of PVDF, the delamination of aqueous processed CMC-based electrodes were attempted using the chemical separation. In this case, by referring to the Hansen space of CMC, it's known that removing the binding forces between the CAM and the current collector is complicated by only using water.[36,59] Using a solution of 5% of carbamide (NH_2CONH_2) in water allows easy delamination due to the substance's high solubility affinity. Nonetheless, besides its good separation efficiency, once the recovered material was analyzed, it was found that the carbamide was attached to the CAM, requiring the removal of the same (Fig. S1†). Because of this, the approach was not pursued further. Consequently, the aqueous processed electrodes were separated using mechanical and thermal techniques.

For the chemical separation of the LNMO material from organic processed PVDF-based electrode scraps, Cyrene was chosen as an environmentally benign solvent for dissolving the PVDF binder, based on the similarity of their Hansen solubility parameters (dispersion, polar, and hydrogen bonding).[36,60] An adequate temperature is required to accelerate and inhibit the PVDF's reprecipitation for the separation process. Binder removal and consequent electrode delamination occur when the sample is introduced into the heated Cyrene solution under
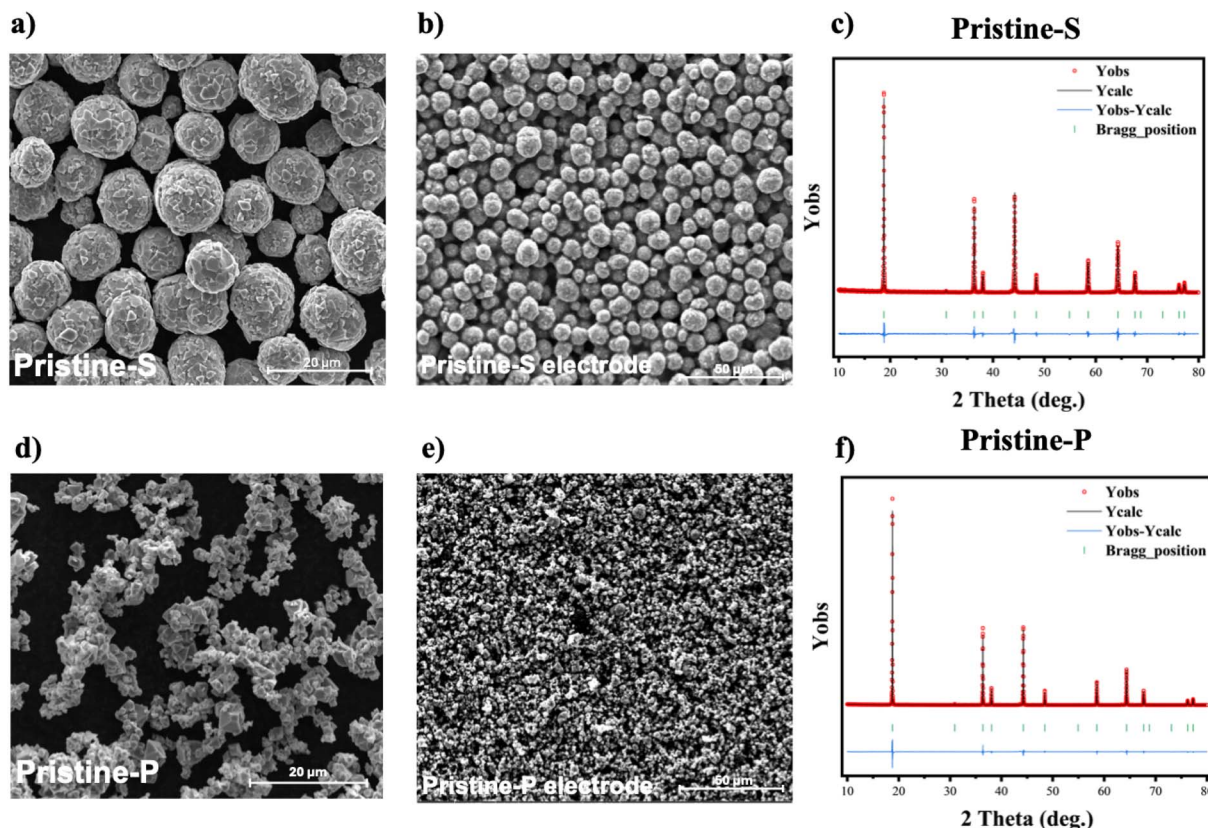
Fig. 3 SEM micrographs and Le Bail fits of the XRD patterns of pristine LNMO powders and electrodes of the type Pristine-S (a–c) and type Pristine-P (d–f).

agitation (Fig. S2a†). This disrupts the bonds formed by the binder between the active material and the surface of the current collector, as schematically shown in Fig. 2(b), allowing the intact recovery of the current collectors, see (Fig. S2b†). The electrodes delaminated with the chemical separation technique report a recovery rate (RR) of 88 ± 2% from the Pristine-S electrodes *vs.* 85 ± 2% for Pristine-P electrodes, with no major influence of the LNMO type in the RR of the recovered materials. It is noteworthy that, while the Cyrene solution is not saturated, the separation process can be performed several times with the same solution. The resulting solution contains a mixture of Cyrene, PVDF, and carbon residue (Fig. S2c†).

Various parameters govern the mechanical separation process, including the choice of solvent, temperature, and power/duration of the applied force.[61] The longitudinal waves produced by the ultrasound are absorbed in the surface of the electrodes, creating an aggregate of the cathode particles that causes the breaking of the bonds between the cast material and the current collector, allowing progressive electrode delamination, as illustrated in Fig. 2(c). In the present work, distilled water was selected as a self-evident dispersant for the separation of the aqueous processed CMC-based electrode scraps (Fig. S2d†). It should be noted that while the application of ultrasound is primordial for achieving the delamination of this type of electrodes, elevated sonication energy and prolongued exposition time result in the decomposition of the aluminum

current collector, contaminating the recovered product and jeopardizing its electrochemical performance.[62] Adequately adjusting these parameters maximizes the recovery rate without compromising the purity (Fig. S2e†). The electrodes recovered by the mechanical separation report a RR of 78 ± 4% for Pristine-P electrodes, presenting evident remnants of electrode cast on the Al current collector (Fig. S2f†). At the same time, an increased value of 90 ± 5% was obtained for the material recovered from the Pristine-S electrodes, presenting an enhanced delamination.

For the thermal separation, two parameters were considered: (i) the degradation temperature of the conductive carbon and the binder, and (ii) the phase transition temperature of the LNMO from a TM-disordered spinel phase (SG: $Fd\bar{3}m$) to a TM-ordered one ($P4_332$), which occurs around 700 °C in air.[63] A TGA was conducted on the aqueous processed Pristine-S electrode to determine the temperature required to completely remove the polymeric binder and conductive carbon (Fig. S3†). The results show several relevant temperature regions. Mass losses occur between 63–180 °C associated with humidity loss. At around 220 °C the Kynar latex[64] and volatile matter are released. Furthermore, at approximately 460 °C the CMC is removed.[65] The carbonaceous content combusts at around 659 °C (Fig. S3a†). Based on these results, a temperature value of 650 °C was chosen for thermal separation, with one hour of annealing under air. Once the thermal process is complete, the cooled-

This journal is © The Royal Society of Chemistry 2025

J. Mater. Chem. A, 2025, **13**, 2690–2706 | **2697**

down material can be quickly recovered by gently hand scratching the electrode (Fig. S2g–h†); see Fig. 2(d). It should be noted that temperatures exceeding 700 °C can cause melting and degradation of the Al current collector or phase transition of the CAM (Fig. S2i†). The result reveals consistent RRs for samples separated by thermal routes, averaging around 91 ± 3% from the pristine electrodes prepared with LNMO-S and LNMO-P types materials.

After performing the separation processes, the recovered powders were thoroughly characterized to verify the preservation of the CAM integrity and identify potential impurities. In the following, the recovered materials are labeled according to the employed separation method and LNMO type used as CAM: Chemical-P, Mechanical-P, and Thermal-P *vs.* Chemical-S, Mechanical-S, Thermal-S.

SEM images of the recovered LNMO powders (Fig. 4) reveal no apparent changes in morphology, particle cracking, or other alterations compared to pristine materials (Fig. 3a and c). However, the materials obtained from the chemical and mechanical separation techniques exhibit certain residual content, marked with red circles in Fig. 4. This suggests that the purification steps applied after these separations could not thoroughly remove the conductive carbon and binders. The residuals were characterized by SEM-EDX and elemental analysis, showing a carbonaceous nature in both cases. In contrast, the materials recovered by the thermal method did not show any visible traces of residuals.

Particle Size Analysis (PSA) (Fig. S4†) supports the SEM observations, revealing a broadening of the size distribution (Dv90) as well as an increase in median particle size (Dv50) for

the resultant powders of the Chemical-S and Mechanical-S compared to the Pristine-S. This suggests that remnants of the separation process adhere to the spherical-shaped LNMO particles' surface, leading to agglomeration, as observed in SEM. Notably, these changes are much less pronounced in the recovered LNMO-S samples, although a slight broadening and an increase in the median are also observed (see Fig. S4†).

The residual content was quantified using elemental analysis (Table S5†), which confirmed that the thermal separation method yielded materials with the highest purity, devoid of any undesired elements. In contrast, the chemical and mechanical separation techniques revealed an evident correlation between the type of LNMO and residual content. Specifically, the LNMO-S type exhibits a higher residual content than LNMO-P. This was observed in both Chemical-S (6.79 ± 0.01) and Mechanical-S (4.94 ± 0.01), which had significantly higher residual content than their polygonal counterparts, Chemical-P (2.89 ± 0.01) and Mechanical-P (1.73 ± 0.01). Consistent with these findings, SEM imaging and PSA also indicate a higher carbon residual content in LNMO-S recovered samples compared to LNMO-P recovered ones.

Fig. 5 shows that the XRD patterns of the different recovered LNMO-S (a) and LNMO-P (b) are similar to their pristine counterparts, indicating no significant changes. No rock salt impurities or other new crystalline phases were observed. Le Bail fits were performed to determine possible changes in the cell parameters of the samples (Fig. S5†). A slight decrease in lattice parameter value was noted, with 0.14% reduction for Thermal-S and 0.11% for Thermal-P, which could be attributed to spatial optimization upon TM ordering.[66]
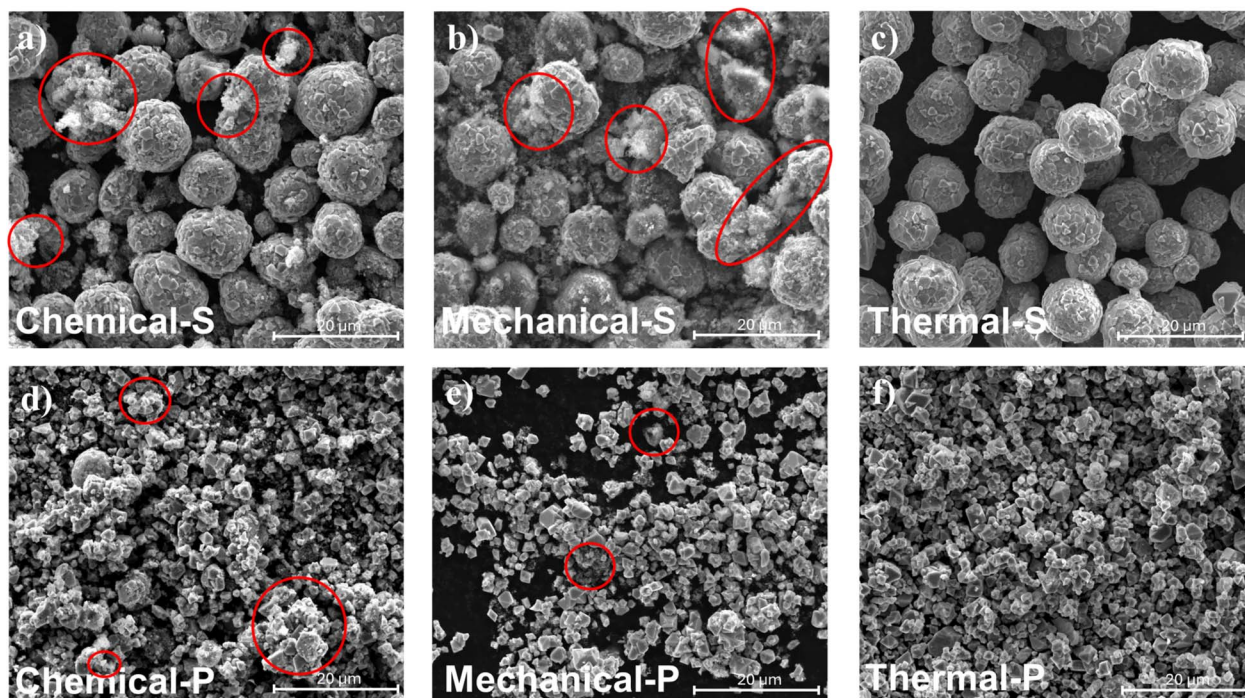

Fig. 4 SEM images of LNMO-S (top) and LNMO-P (bottom) particle materials recovered by chemical (left), mechanical (center), and thermal (right) separation techniques. Red circles mark the presence of undesired residuals.

2698 | *J. Mater. Chem. A*, 2025, **13**, 2690–2706

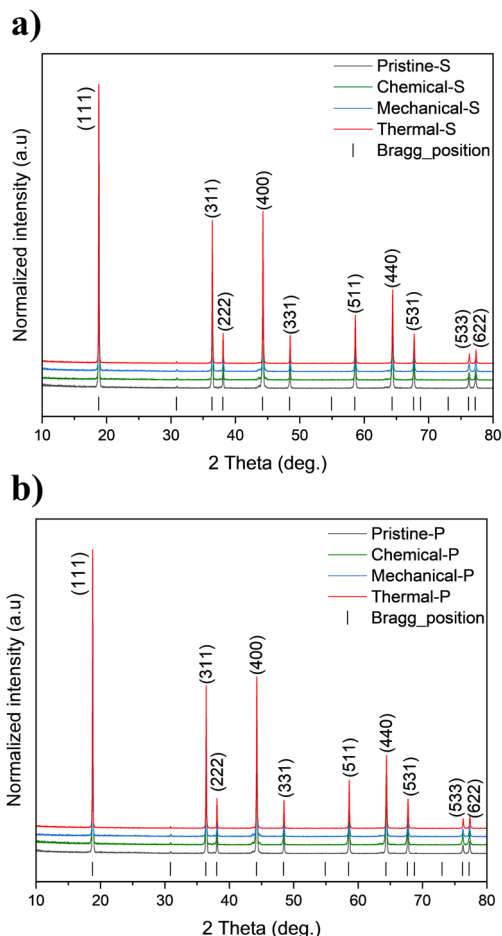This journal is © The Royal Society of Chemistry 2025

Fig. 5 XRD patterns of the different (a) LNMO-S and (b) LNMO-P samples. The black, green, blue, and red (from bottom to top) correspond to the pristine, chemical, mechanical, and thermal separated materials, respectively. Grey vertical lines correspond to the Bragg position for LNMO $Fd\bar{3}m$ spinel.
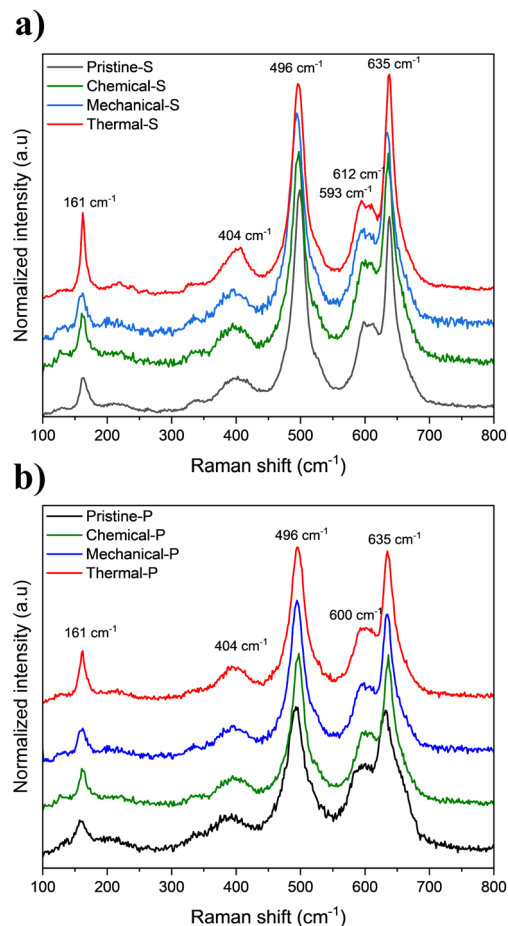

Fig. 6 Raman spectra of the different (a) LNMO-S and (b) LNMO-P samples. The black, green, blue, and red (from bottom to top) correspond to the pristine, chemical, mechanical, and thermal separated, respectively.

The ICP results are summarized in Table S4,† which shows that Mn and Ni molar ratios change depending on the separation treatment and sample type. A reduction in the Mn/Li is observed for the resulting materials from the chemical separation technique. This could be attributed to partial Mn leaching during the separation process, possibly related to the additional rinsing steps or the Cyrene treatment.[39,49] In contrast, the recycled aqueous processed LNMO-S and LNMO-P type present values within the error to the pristine composition. Interestingly, no significant change of Ni stoichiometry is observed in the recovered materials, maintaining a Ni-deficient composition (Ni/Li ≈ 0.44).

Raman spectroscopy was conducted on the recovered LNMO samples to complement structural analysis (Fig. 6). This technique is highly sensitive to the coordination geometry of manganese (Mn) within MnO_6 octahedra or lithium (Li) within LiO_4 tetrahedra, as well as to the oxidation state of the transition metal oxide in the spinel compound (Li^+–O, Ni_2^+–O, Mn_3^+–O).[67,68] Distinctive features are observed in these LNMO samples:

(1) The stretching vibration of Mn–O within the MO_6 octahedral phase at 635 cm^{-1} (2) the stretching vibrations of Ni–O are evidenced in the bands at 404 and 496 cm^{-1} (3) the characteristic band of 600 cm^{-1} corresponds to the T_{2g} vibration mode characteristic of the spinel structure compounds (4) the 160 cm^{-1} related to the Li–O vibrational and coherent domain size.[69]

These characteristic peaks indicate the presence of different cations (Ni^{2+}, Mn^{3+}, and Mn^{4+}) in the sample occupying the same site, leading to different local environments. The higher intensity of 161 cm^{-1} band for Thermal-S and Thermal-P recovered samples suggests an increase in TM ordering, also reflected by a slight lattice contraction (*vide supra*, XRD), as a consequence of phase transition upon heat treatment.[70] However, the LNMO disordered phase remains prevalent, as none of the characteristic peaks of the TM ordered phase (*e.g.* at around ≈225 cm^{-1}) emerge.[63] In this regard, the observed splitting of the T_{2g} band in all the spherical samples (600 cm^{-1}) indicates a consistent slight difference in the TM order compared to the polygonal samples.[71]

Besides the vibrational bonds of LNMO, extended Raman spectra also reveal the two characteristic peaks of carbon in the

chemical and mechanical recovered samples (Fig. S6†), reaffirming the presence of carbon residuals detected by SEM and elemental analysis. Notably, the D band peak at around 1350 cm⁻¹, attributed to defects in the C–C lattice structure, and the G band peak at around 1600 cm⁻¹ corresponding to the graphitized carbon structure.[72] The band ratio for the organic processed and aqueous processed electrodes LNMO are in good agreement with those of their respective carbon additives C65 and C45, precluding the presence of other carbon types.

The solid state ^{7}Li NMR spectra of the Thermal-S and Thermal-P recovered LNMO samples reveal various peaks at 1088, 1010, 935, 834, and 736 ppm, see Fig. S7.† These can be attributed to the existence of different local Li environments with varying Ni/Mn local coordination ratios, characteristic for TM disordered LNMO.[73] Globally, the paramagnetic Li environments are preserved upon thermal treatment, and no distinguishable increase in diamagnetic Li species (e.g. Li_2O, Li_2CO_3 are observed). The slight increase in the intensity ratio of the 1010 ppm peak, attributed to the ideally TM-ordered stoichiometric environment of the heat treated compared to the pristine, suggests that it promotes TM ordering, in line with observations from Raman spectroscopy.

The electrochemical performance of the pristine scrap electrodes was compared with that of the new aqueous electrodes prepared with the different LNMO recycled powders. The results are summarized in Fig. 7 and Table S5.† In all charge/discharge curves, the three typical redox plateaus are observed. First, the plateau around 4 V vs. Li/Li⁺ is attributed to the redox reaction of Mn^{3+}/Mn^{4+}, corresponding to Mn^{3+} occupancy.[73,74] The

following two plateaus between 4.7–4.8 V are attributed to the redox reaction of Ni, which correspond to Ni^{2+}/Ni^{3+} and Ni^{3+}/Ni^{4+} couples, respectively. No additional redox phenomena nor major changes in the Mn and Ni redox features are observed, as highlighted in corresponding dq/dV plots, see Fig. 7(c) and (f).

In general, the charge profiles show that the contribution to the system's overall capacity from the Mn^{3+}/Mn^{4+} redox couple slightly varies for the two different LNMO types investigated. To account for mass error-induced variations, we normalized the discharge capacities (Fig. S8 and S9a–h†). This allows the comparison of the profiles more accurately. The normalized profiles indicate high consistency, and the difference in the capacity values can be attributed to additional residual contents or minor errors in determining the active material loading. The quantification of the Mn^{3+} redox contribution within the system can be calculated with the 4 V capacity. This value relates directly to the amount of Mn^{3+} in the LNMO structure. The results from eqn (2) of the different samples indicate that, on average, the 4 V capacity contribution is higher for the LNMO-P type samples (22%) than for the LNMO-S type samples (15%) (Table S6†). From this evaluation, the stoichiometric ratio of Ni and Mn within the active materials can be redetermined (eqn (3) and (4)) and contrasted with the ICP results (Table S4†). In this regard, both ICP and electrochemical compositional analyses agree that Mn excess is prevalent in all the LNMO samples, consistent with previous study results,[73] and confirms TM ratio preservation after the CAM recovery from the electrode scraps.

Besides the Mn^{3+} content, an upshift of the $Ni^{2+/3+}$ plateau, best observed in the corresponding $\delta Q/\delta V$ in Fig. 7(c) and (f)
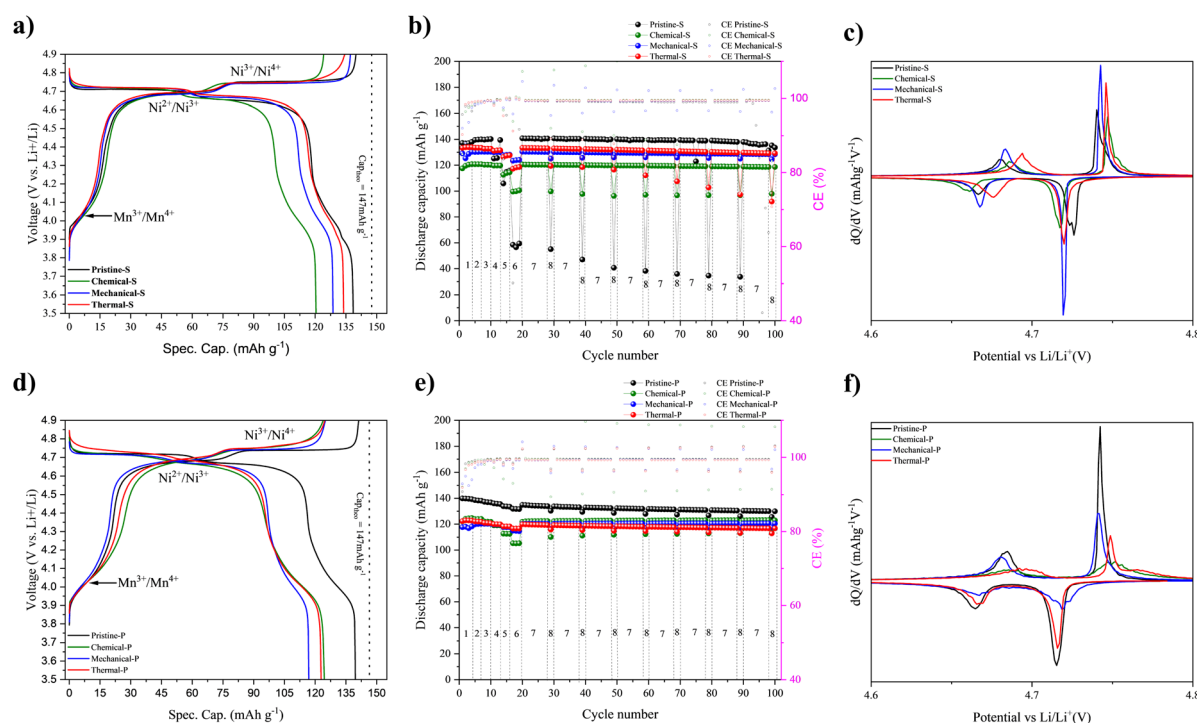

Fig. 7 (Left) Voltage profile of the third cycle, center: capacity and coulombic efficiency, and right $\delta Q/\delta V$ for the LNMO-S (top) and LNMO-P (bottom) samples. The black, green, blue, and red (from bottom to top) correspond to the base pristine and compared chemical, mechanical, and thermal recovered samples respectively.

2700 | J. Mater. Chem. A, 2025, **13**, 2690–2706

This journal is © The Royal Society of Chemistry 2025

(also see ESI Fig. S8 and S9† for more detailed analysis) can be evinced. This narrowing of the nickel voltage plateaus can be attributed to the influence of the TM order.[75] The results obtained indicate that the CAM effectively corresponds to the TM-disordered LNMO phase, as the values are similar to those previously reported for TM-disordered LNMO samples[76] and by the results obtained by Raman and ssNMR. It is worth noticing that there is a common misconception that the TM order and the Mn content are firmly linked, but recent works have rebutted this.[75,77]

Regarding cycling performance, the electrodes using the recovered samples provide reversible capacities of >120 mA h g^{-1} after formation cycles (i.e. the initial cycles required for the battery to stabilize its capacity). The electrodes maintain stable cycling during rate capability and capacity retention testing, with less than 3% of capacity loss after 100 cycles; see Fig. 7(b) and (e), as well as Table S6† for more details. The high reversibility of the lithiation delithiation reaction is exemplified by the coulombic efficiency (CE) values converging towards 100% after completion of formation cycles, see Fig. 7(b) and (e) right purple y-axis.

It should be noted that both pristine samples show a higher capacity than the recovered ones, which is attributed to an improved electrode formulation and processing of the scrap electrodes with respect to the electrodes cast with the recovered CAMs. Meanwhile, their increased areal loading results in a more pronounced capacity decrease at an elevated rate (>1C). Overall, the different separation techniques do not notably affect the electrochemical behavior of the samples, and only the recovered materials with carbon residuals present a reduced specific capacity. This loss in specific gravimetric capacity can be primarily attributed to the additional dead weight of the residuals, but other detrimental effects, such as Li trapping or overpotential growth, can not be excluded.

4 Discussion

The findings obtained from the thorough characterization of the recovered LNMO samples allow a comprehensive comparison of the three different separation techniques. Six key indicators were compared using dedicated radar plots for each separation technique, and both investigated CAMs types, see Fig. 8. RR represents the overall material recovery yield of the different separation methods. The purity reflects the percentage of desired active material within the recovered powder, as explained in the experimental section. The capacity retention reflects the cycling ability of the material and is calculated by comparing the cycling after formation with the last cycle. The normalized capacity indicator is reported as a percentage of a reversible discharge capacity relative to that of the pristine electrode. To evaluate the feasibility of the studied recycling techniques, their convenience indicator was assessed, which contains each technique's processing time and ease of procedure, normalized to a 100% scale. The energy input for each separation process was calculated using the equations presented in Section 2.6. The results were normalized to the least energy-intensive approach (i.e., mechanical separation ≈4.26

MJ) and plotted in a percentage scale with the highest scores reflecting the lowest energy input.

The comparison of the different factors reveals that the LNMO type influenced several outcome indicators, i.e., recovery rate, convenience, and purity. For the RR, the most salient difference is observed for the mechanical separation technique, for which LNMO-P achieved considerably lower values than LNMO-S (78% vs. 90%). In the chemical separation technique, the differences are less pronounced and inversed, with LNMO-S type exhibiting slightly lower values than LNMO-P type. Thermal separation reveals only minor differences between the two types of LNMO. To explain the influence of particle morphology on the separation efficiency, adhesion tests comparing aqueous-processed LNMO-S and LNMO-P electrodes were conducted. However, the results show no significant difference in the global adhesion force (Fig. S10†). It is hypothesized that the observed remnants on the current collector may be related to locally higher inter-particle adhesion force for LNMO-P, leading to a lower recovery rate than for LNMO-S. Whether the differences in the separation of the two different LNMO morphologies are related to the different particle size (10 vs. 1 μm), their shape (spherical vs. polygonal), and/or exposed surface facets can not be answered with certainty. It should be noted that increasing the energy and time of sonication can increase the RR; however, this comes at the risk of inducing aluminum contamination into the recovered material and promoting localized surface damage, such as pitting, which may compromise the integrity of the battery components, as previously discussed by ref. 40 and 78.

Overall, the RR results are in the vicinity of 90%, reflecting an effective removal of the electrode material for the three separation techniques on both types of LNMO. Although comparability of recovery rate to other studies is limited due to differences in chemistry, formulation, and state-of-life of the materials to be recycled, similar values have been reported for chemical (85%),[16] mechanical (>98%)[78] and thermal separation techniques (80–95%, 75%).[17,41] In regard of the purity indicator, the highest scores were achieved with the thermal separation technique, reflecting the absence of residuals in the recovered powders. Meanwhile, mechanical and chemical separation techniques attain purity values of ≥93%.

The electrochemical performance of the recovered materials appears consistent over cycling, with capacity retention similar for all the LNMOs types, showing stable electrochemical cycling, which underlines the benign nature of the applied direct recycling approach, resulting in a retention of the capacity of at least 97%. Regarding capacity, the values obtained from the mechanical and thermal separation techniques are closely tied, with the highest values obtained from Thermal-S and Mechanical-S, reaching 95% and 93% of the pristine electrode's specific capacity, respectively. The performance aligns with the results presented in the works of,[38,39,42] who report capacities of more than 90% when testing recycled materials from other chemistries.

Differences in the convenience parameter between the LNMO types reflect the impact of their respective morphology, processing time, and number of steps on the required

This journal is © The Royal Society of Chemistry 2025

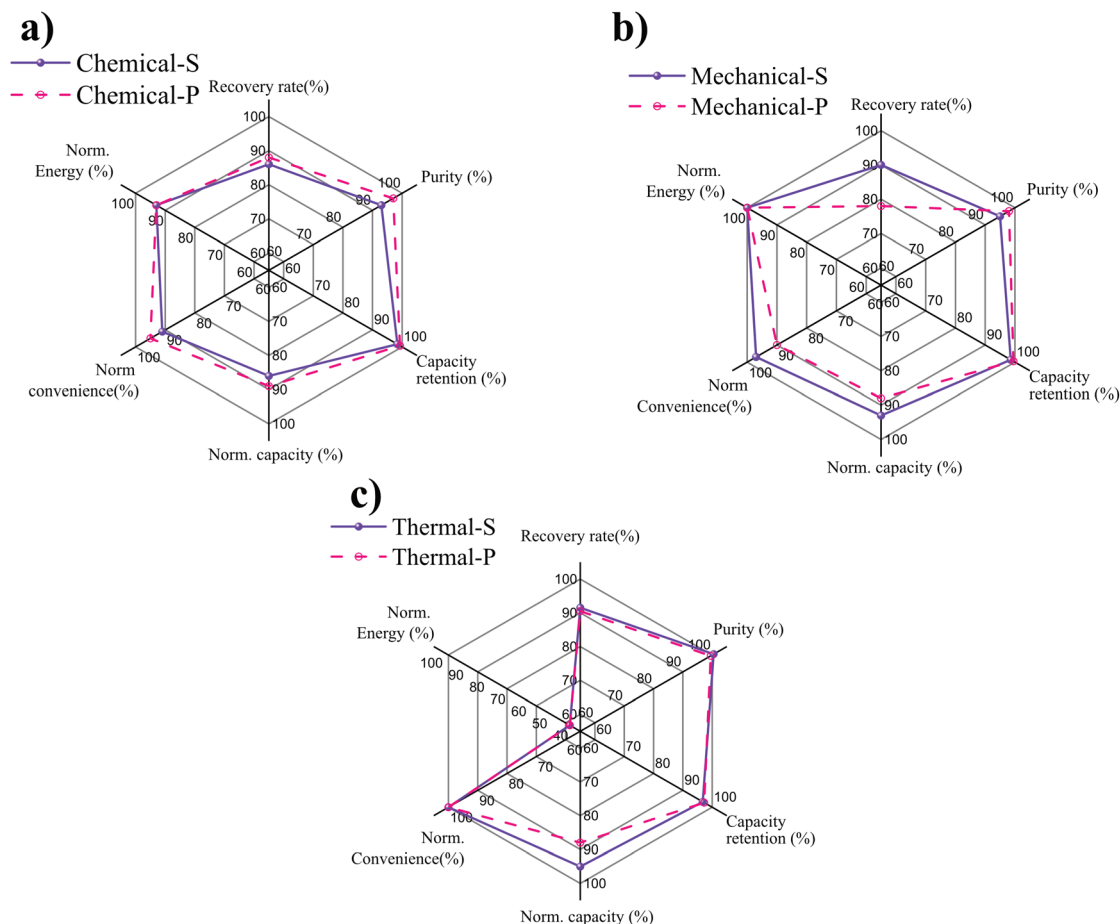J. Mater. Chem. A, 2025, 13, 2690–2706 | 2701

Fig. 8 Spider plots comparing the recovery rate (RR) (%), purity (%), capacity retention (%), norm capacity (%), norm convenience (%), and norm energy (%) for both LNMO-S and LNMO-P types results investigated for the different separation techniques; chemical (a), mechanical (b), and thermal (c).

separation technique. The thermal separation technique achieves the best results due to its ease of delamination, one-step process, and the absence of residuals in the resultant materials. At the same time, mechanical and chemical separation techniques require extra purification steps, take longer time, and need extra considerations for the separation process. However, according to our preliminary energy consumption estimation, the thermal separation technique requires twice as much energy as the other two separation techniques. It also bears the risk of HF release for PVDF-based binders, making monitoring and treating fume exhausts necessary. On the other hand, thermal separation doesn't involve the use of solvents or byproducts, which require waste management at an industrial scale, as in the mechanical and chemical separation techniques.

Summarizing these proposed performance metrics, the thermal separation technique is considered the best of the three separation techniques for LNMO scrap electrodes tested here. It offers the highest recovery rates and purities independent of particle morphology. Regarding ease and time, the thermal separation also excels since it does not require additional purification or drying steps, as depicted in Fig. 2. However, in

terms of electrochemical performance, the thermal separated samples deliver higher absolute capacity values and similar capacity retentions as the samples from other separation techniques.

It is important to remark that this comparison is established from a basic evaluation of the inputs and outputs of the processes. A more systematic evaluation, including detailed energy expenses, development/operational cost, technology transfer, regulatory compliance, process optimization, and risk assessment, must be considered to determine the viability of the three separation routes at the industrial scale; however, this lies out of the scope of this work. One of the aspects to consider for their up-scaling is the carbonaceous residual content. While this poses no significant drawback for the recycling objectives of this work, as the same material is used in the reprocessing step, in a real case scenario, it would be necessary to effectively identify the amount and characteristics of the carbon residue in the recovered material to take it into account for the electrode formulation recipe. Also, it is necessary to mechanically prepare the recovered samples to obtain a uniform powder that allows a homogeneous dispersion in the slurry.

2702 | J. Mater. Chem. A, 2025, 13, 2690–2706

This journal is © The Royal Society of Chemistry 2025

To assess the feasibility of the previously tested methodologies at a larger scale, electrode scraps obtained from two industrial pilot lines were employed to demonstrate the effectiveness and performance of the proposed separation techniques on real-case materials. These aqueous-processed electrodes manufactured with LNMO-S type CAM powders are labeled Pristine-SA and Pristine-SS. The CAM was recovered from these two types of electrodes using the thermal and mechanical separation techniques and labeled accordingly. Detailed results can be found in Fig. S11 and S12.† RR are similar to those of previously tested lab-made ones, with approximately 97% for thermal and 91% for mechanical separated samples. Analogous to lab prepared laminates, these samples show the same tendency of nearly complete removal of residual for the thermal separated samples and the presence of residual for the mechanical separated ones, as depicted by SEM analysis (Fig. S13†). The electrochemical data of the electrodes prepared with the recycled material showcase the process's transferability and reproducibility, presenting a satisfactory electrochemical performance of 129 mA h g^{-1} for the Mechanical-SS (140 mA h g^{-1} for the Pristine-SS) and of 135 mA h g^{-1} for the Thermal-SA (137 mA h g^{-1} for the Pristine-SA) with no capacity decay or unexpected behaviors; those results are consistent with the previous for the lab-made electrodes.

5 Conclusion

This work successfully demonstrates, for the first time, the feasibility of applying a direct recycling method for the recovery and reuse of the LNMO cathode material from scrap battery electrodes. The resulting materials do not show extensive chemical modifications while being able to be reused directly in the preparation of new electrodes. We observed apparent differences between the three separation techniques, chemical, mechanical, and thermal, in terms of the purity of recovered material, convenience, and energy consumption when applied to two distinct LNMO types (LNMO-S and LNMO-P), prepared with two different binder types: CMC (aqueous-processed) and PVDF (organic-processed). Lab-scale tests were validated on commercial-scale electrodes, confirming the scalability of these methods.

The thermal method provides the highest recovery yield and the most straightforward processing. The recovered materials from the chemical and mechanical separation techniques contain certain amounts of conductive carbon and binder residuals that require additional sample processing. Nevertheless, all the separation techniques enable the recovery of the metallic current collector but only the chemical and mechanical techniques, with further processing, allow the recovery of the binder and conductive carbon. The recycled materials demonstrate satisfactory electrochemical performance similar to that of pristine samples, with no significant alterations of the intrinsic properties of the LNMO samples, such as TM ordering, storage ability, or composition. The presence of carbonaceous residuals affects the specific gravimetric capacity due to an overestimation of active mass loading.

Additional techno-economic analyses, such as life-cycle assessments (LCA), should be envisioned to allow the evaluation of the here presented methods' broader viability. It is also crucial to test the performance of recovered LNMO within complete cell systems. As LNMO technology enters the market, further development of these separation techniques is needed to adapt them to the needs of EoL batteries, which will likely require state-of-health estimation and additional rejuvenation steps.

Our findings highlight the potential of direct recycling to reduce waste, improve sustainability, and bolster competitiveness in battery manufacturing by sourcing CAM from discarded scrap materials.

Conflicts of interest

There are no conflicts to declare.

Acknowledgements

References

1 M.-M. Titirici, et al., 2024 roadmap for sustainable batteries, J. Phys. Energy, 2024, 12–20.

2 E. Union. Regulation (EU) 2023/1542 of the European Parliament and of the Council of 12 July 2023 concerning Batteries and Waste Batteries, Amending Directive 2008/98/EC and Regulation (EU) 2019/1020 and Repealing Directive 2006/66/EC (Text with EEA relevance), 2023, https://eur-lex.europa.eu/eli/reg/2023/1542/oj.

3 Q. Hoarau and E. Lorang, An assessment of the European regulation on battery recycling for electric vehicles, Energy Pol., 2022, 162, 112770.

4 G. D. J. Harper, et al., Roadmap for a sustainable circular economy in lithium-ion and future battery technologies, J. Phys. Energy, 2023, 5, 4–10.

5 A. J. Niri, G. A. Poelzer, S. E. Zhang, J. Rosenkranz, M. Pettersson and Y. Ghorbani, Sustainability challenges throughout the electric vehicle battery value chain, Renewable Sustainable Energy Rev.s, 2024, 191, 114176.

6 D. Steward, A. Mayyas and M. Mann, Economics and challenges of Li-ion battery recycling from end-of-life vehicles, Procedia Manufacturing, 2019, 33, 272–279.

This journal is © The Royal Society of Chemistry 2025

J. Mater. Chem. A, 2025, 13, 2690–2706 | 2703

7 C. M. Costa, J. C. Barbosa, R. Gonçalves, H. Castro, F. J. Campo and S. Lanceros-Méndez, Recycling and environmental issues of lithium-ion batteries: Advances, challenges and opportunities, *Energy Storage Mater.*, 2021, **37**, 433–465.

8 X. Sun, H. Hao, P. Hartmann, Z. Liu and F. Zhao, Supply risks of lithium-ion battery materials: An entire supply chain estimation, *Mater. Today Energy*, 2019, **14**, 100347.

9 International Energy Agency, *Batteries and secure energy transitions*, ed. E. Hosker, 2024, available: https://www.iea.org/reports/batteries-and-secure-energy-transitions/status-of-battery-demand-and-supply.

10 J. Neumann, M. Petranikova, M. Meeus, J. D. Gamarra, R. Younesi, M. Winter and S. Nowak, Recycling of Lithium-Ion Batteries—Current state of the art, circular economy, and next generation recycling, *Adv. Energy Mater.*, 2022, **12**, 1–4.

11 A. Zanoletti, E. Carena, C. Ferrara and E. Bontempi, A review of Lithium-Ion battery recycling: Technologies, sustainability, and open Issues, *Batteries*, 2024, **10**, 38.

12 L. Gaines, Lithium-ion battery recycling processes: Research towards a sustainable course, *Sustainable Mater. Technol.*, 2018, **17**, 1–7.

13 M. Zhou, B. Li, J. Li and Z. Xu, Pyrometallurgical Technology in the Recycling of a Spent Lithium Ion Battery: Evolution and the Challenge, *ACS ES&T Eng.*, 2021, **1**, 1369–1382.

14 K. Davis and G. P. Demopoulos, Hydrometallurgical recycling technologies for NMC Li-ion battery cathodes: current industrial practice and new Ramp;D trends, *RSC Sustainability*, 2023, **1**, 1932–1951.

15 T. Yang, D. Luo, A. Yu and Z. Chen, Enabling future closed-loop recycling of spent lithium-ion batteries: direct Cathode regeneration, *Adv. Mater.*, 2023, **35**, 1–10.

16 M. Ahuis, A. Aluzoun, M. Keppeler, S. Melzig and A. Kwade, Direct recycling of lithium-ion battery production scrap – Solvent-based recovery and reuse of anode and cathode coating materials, *J. Power Sources*, 2023, **593**, 233995.

17 M. Mancini, M. F. Hoffmann, J. Martin, D. Weirather-Köstner, P. Axmann and M. Wohlfahrt-Mehrens, A proof-of-concept of direct recycling of anode and cathode active materials: From spent batteries to performance in new Li-ion cells, *J. Power Sources*, 2024, **595**, 233997.

18 G. Ji, D. Tang, J. Wang, Z. Liang, H. Ji, J. Ma, Z. Zhuang, S. Liu, G. Zhou and H.-M. Cheng, Sustainable upcycling of mixed spent cathodes to a high-voltage polyanionic cathode material, *Nat. Commun.*, 2024, **15**, 1–10.

19 L. Gaines, Q. Dai, J. T. Vaughey and S. Gillard, Direct Recycling Ramp;D at the ReCell Center, *Recycling*, 2021, **6**, 1–18.

20 M. Machala, X. Chen, S. P. Bunke, G. Forbes, A. Yegizbay, J. De Chalendar, I. Azevedo, S. M. Benson and W. Tarpeh, Life Cycle Comparison of Industrial-Scale Lithium-Ion Battery Recycling and Mining Supply Chains, *SSRN Electron. J.*, 2022, 1–26.

21 R. Madge, A. Jarvis, W. L. Da Silva, L. L. Driscoll, P. A. Anderson and P. R. Slater, Up-cycling of low value

end-of-life cathode material into next generation cathode materials, *RSC Sustainability*, 2024, **2**, 1408–1417.

22 A. J. Green, E. H. Driscoll, P. A. Anderson, E. Kendrick and P. R. Slater, High-power ecycling: upcycling to the next generation of high-power anodes for Li-ion battery applications, *J. Mater. Chem. A*, 2024, **12**, 7321–7328.

23 P. Zhu, E. H. Driscoll, B. Dong, R. Sommerville, A. Zorin, P. R. Slater and E. Kendrick, Direct reuse of aluminium and copper current collectors from spent lithium-ion batteries, *Green Chem.*, 2022, **25**, 3503–3514.

24 H. Ji, J. Wang, J. Ma, H.-M. Cheng and G. Zhou, Fundamentals, status and challenges of direct recycling technologies for lithium ion batteries, *Chem. Soc. Rev.*, 2023, **52**, 8194–8244.

25 X. Yu, W. Li, V. Gupta, H. Gao, D. Tran, S. Sarwar and Z. Chen, Current challenges in Efficient Lithium-Ion batteries' recycling: A perspective, *Global Challenges*, 2022, **6**, 1–8.

26 V. Gupta, M. Appleberry, W. Li and Z. Chen, Direct recycling industrialization of Li-ion batteries: The pre-processing barricade, *Next Energy*, 2024, **2**, 100091.

27 D. L. Thompson, J. M. Hartley, S. M. Lambert, M. Shiref, G. D. J. Harper, E. Kendrick, P. Anderson, K. S. Ryder, L. Gaines and A. P. Abbott, The importance of design in lithium ion battery recycling – a critical review, *Green Chem.*, 2020, **22**, 7585–7603.

28 S. Scott, Z. Islam, J. Allen, T. Yingnakorn, A. Alflakian, J. Hathaway, A. Raste-garpanah, G. D. J. Harper, E. Kendrick, P. A. Anderson, J. Edge, L. Lander and A. P. Abbott, Designing lithium-ion batteries for recycle: The role of adhesives, *Next Energy*, 2023, **1**, 100023.

29 B. Andreas, L. Martin, T. Chuldt, G. Siccardo and N. Vekic, *Battery recycling takes the driver's seat*, 2023, https://www.mckinsey.com/industries/automotive-and-assembly/our-insights/battery-recycling-takes-the-drivers-seat#/.

30 . Strategy University, P. A, *EU recycling market The EU recycling market-a viable and sustainable business*, 2023, https://www.strategyand.pwc.com/de/en/industries/automotive/recycling-european-battery.html.

31 N. Hayagan, I. Gaalich, P. Loubet, L. Croguennec, C. Aymonier, G. Philippot and J. Olchowka, Challenges and perspectives for direct recycling of electrode scraps and End-of-Life lithium-ion batteries, *Batteries Supercaps*, 2024, **7**, 1–4.

32 L. Gaines, J. Zhang, X. He, J. Bouchard and H. E. Melin, Tracking flows of End-of-Life battery materials and manufacturing scrap, *Batteries*, 2023, **9**, 1–21.

33 Y. Ji, E. E. Kpodzro, C. T. Jafvert and F. Zhao, Direct recycling technologies of cathode in spent lithium-ion batteries, *Clean Technol. Recycl.*, 2021, **1**, 124–151.

34 T.-W. Wang, T. Liu and H. Sun, Direct recycling for advancing sustainable battery solutions, *Mater. Today Energy*, 2023, **38**, 101434.

35 Y. Bai, N. Muralidharan, J. Li, R. Essehli and I. Belharouak, Sustainable Direct Recycling of Lithium-Ion Batteries via Solvent Recovery of Electrode Materials, *ChemSusChem*, 2020, **13**, 5664–5670.

2704 | *J. Mater. Chem. A*, 2025, **13**, 2690–2706

This journal is © The Royal Society of Chemistry 2025

36 C. M. Hansen, *Hansen Solubility Parameters*, CRC Press, 2007.

37 Y. Bai, R. Essehli, C. J. Jafta, K. M. Livingston and I. Belharouak, Recovery of Cathode Materials and Aluminum Foil Using a Green Solvent, *ACS Sustain. Chem. Eng.*, 2021, **9**, 6048–6055.

38 M. M. Gnutzmann, A. Makvandi, B. Ying, J. Buchmann, M. J. Lüther, B. Helm, P. Nagel, M. Peterlechner, G. Wilde, A. Gomez-Martin, K. Kleiner, M. Winter and J. Kasnatscheew, Direct Recycling at the Material Level: Unravelling Challenges and Opportunities through a Case Study on Spent Ni-Rich Layered Oxide-Based Cathodes, *Adv. Energy Mater.*, 2024, 1–14.

39 Y. Bai, W. B. Hawley, C. J. Jafta, N. Muralidharan, B. J. Polzin and I. Belharouak, Sustainable recycling of cathode scraps via Cyrene-based separation, *Sustainable Mater. Technol.*, 2020, **25**, 1–7.

40 C. Lei, I. Aldous, J. M. Hartley, D. L. Thompson, S. Scott, R. Hanson, P. A. Anderson, E. Kendrick, R. Sommerville, K. S. Ryder and A. P. Abbott, Lithium ion battery recycling using high-intensity ultrasonication, *Green Chem.*, 2021, **23**, 4710–4715.

41 T.-O. Folayan, A. L. Lipson, J. L. Durham, H. Pinegar, D. Liu and L. Pan, Direct recycling of blended cathode materials by froth flotation, *Energy Technol.*, 2021, **9**, 2100468.

42 X. Chen, S. Li, Y. Wang, Y. Jiang, X. Tan, W. Han and S. Wang, Recycling of LiFePO$_4$ cathode materials from spent lithium-ion batteries through ultrasound-assisted Fenton reaction and lithium compensation, *Waste Manage.*, 2021, **136**, 67–75.

43 Z. Tong, X. Ren, M. Ni, X. Bu and L. Dong, Review of Ultrasound-Assisted Recycling and Utilization of Cathode Materials from Spent Lithium-Ion Batteries: State-of-the-Art and Outlook, *Energy Fuels*, 2023, **37**, 14574–14588.

44 Y. Ji, C. T. Jafvert, N. N. Zyaykina and F. Zhao, Decomposition of PVDF to delaminate cathode materials from end-of-life lithium-ion battery cathodes, *J. Cleaner Prod.*, 2022, **367**, 133112.

45 X. Zhang, Q. Xue, L. Li, E. Fan, F. Wu and R. Chen, Sustainable Recycling and Regeneration of Cathode Scraps from Industrial Production of Lithium-Ion Batteries, *ACS Sustainable Chem. Eng.*, 2016, **4**, 7041–7049.

46 H. Oubaha, L. Fkhar, R. Cloots, F. Boschini and A. Mahmoud, Direct NCA Cathode Active Materials Recycling from Spent Li-Ion Batteries: Solvent-Free Recovery and Healing by Heat Treatment, *ACS Sustainable Resour. Manage.*, 2024, **1**, 1791–1801.

47 E. C. Giles, A. Jarvis, A. T. Sargent, P. A. Anderson, P. K. Allan and P. R. Slater, Direct recycling of EV production scrap NMC532 cathode materials, *RSC Sustainability*, 2024, **2**, 3014–3021.

48 M. De Gennaro; B. Ganev; M. Jahn; M. Reynaud; M. Fehse; L. Otaegui; M. Ca-bello; S. Mannori; O. Rahbari 3BeLIEVE: towards delivering the next generation of LMNO Li-Ion battery cells and packs fit for electric vehicle applications of 2025 and beyond. *SAE Technical Papers on CD-ROM/SAE Technical Paper Series* 2021, 1–12.

49 I. Dienwiebel, M. Diehl, B. Heidrich, X. Yang, M. Winter and M. Börner, Enabling aque-ous processing for LINI0.5MN1.5O4-Based positive electrodes in Lithium-Ion batteries by applying Lithium-Based processing additives, *Adv. Energy Sustainability Res.*, 2021, **2**, 2100075.

50 G. Liang, V. K. Peterson, K. W. See, Z. Guo and W. K. Pang, Developing high-voltage spinel LiNi0.5Mn1.5O4 cathodes for high-energy-density lithium-ion batteries: current achievements and future prospects, *J. Mater. Chem. A*, 2020, **8**, 15373–15398.

51 J. Lee, N. Dupre, M. Avdeev and B. Kang, Understanding the cation ordering transition in high-voltage spinel LiNi0.5Mn1.5O4 by doping Li instead of Ni, *Sci. Rep.*, 2017, **7**, 2–5.

52 P. Jehnichen, K. Wedlich and C. Korte, Degradation of high-voltage cathodes for advanced lithium-ion batteries–differential capacity study on differently balanced cells, *Sci. Technol. Adv. Mater.*, 2019, **20**, 1–9.

53 W. Yao, Y. Li, M. Olguin, S. Bai, M. A. Schroeder, W. Li, A. Liu, N. R. Park, B. Bhamwala, B. Sayahpour, G. Raghavendran, O. Borodin, M. Zhang and Y. S. Meng, Stabilizing high temperature operation and calendar life of LiNi0.5Mn1.5O4, *Next Energy*, 2024, **4**, 100136.

54 Morrow Cutting-edge battery technology development | Morrow Batteries, **https://www.morrowbatteries.com/products**.

55 T. Corporation, *Toshiba develops new Lithium-Ion battery with Cobalt-Free 5V Class High-Potential Cathode*, 2021, **https://www.global.toshiba/ww/technology/corporate/rdc/rd/topics/23/2311-02.html**.

56 J. Rodriguez-Carvajal, PHYSICA Recent advances in magnetic structure determination neutron powder diffraction, *Physica B*, 1993, **192**, 113.

57 C. Fink; L. F. Lundegaard; J. W. Høj; J. Højberg; C. F. Elkjaer T. Haldor. *Characterization of High-Voltage Li 1.0 Ni 0.5 Mn 1.5 O 4 and Correspondence between Ni Content in Spinel, Lattice Size and 4V Capacity*. White paper 2022, 1–10.

58 J. Diekmann, C. Hanisch, L. Froböse, G. Schälicke, T. Loellhoeffel, A.-S. Fölster and A. Kwade, Ecological Recycling of Lithium-Ion Batteries from Electric Vehicles with Focus on Mechanical Processes, *J. Electrochem. Soc.*, 2017, **164**, A6184–A6191.

59 J. Lang, H. Zhang, N. Wang, X. Wang, Y. Wang and G. Chen, Applications of the Hansen solubility parameter for cellulose, *BioResources*, 2021, **16**, 7112–7121.

60 J. E. Marshall, A. Zhenova, S. Roberts, T. Petchey, P. Zhu, C. E. J. Dancer, C. R. McElroy, E. Kendrick and V. Goodship, On the Solubility and Stability of Polyvinylidene Fluoride, *Polymers*, 2021, **13**, 1354.

61 L. P. He, S. Y. Sun, X. F. Song and J. G. Yu, Recovery of cathode materials and Al from spent lithium-ion batteries by ultrasonic cleaning, *Waste Manage.*, 2015, **46**, 523–528.

62 R. Zhang, Y. Zheng, Z. Yao, P. Vanaphuti, X. Ma, S. Bong, M. Chen, Y. Liu, F. Cheng, Z. Yang and Y. Wang, Systematic Study of Al Impurity for NCM622 Cathode Materials, *ACS Sustain. Chem. Eng.*, 2020, **8**, 9875–9884.

This journal is © The Royal Society of Chemistry 2025

J. Mater. Chem. A, 2025, **13**, 2690–2706 | **2705**

63 L. Wang, H. Li, X. Huang and E. Baudrin, A comparative study of Fd-3m and P4332 "LiNi0.5Mn1.5O4", *Solid State Ionics*, 2011, **193**, 32–38.

64 A. Brilloni, F. Marchesini, F. Poli, E. Petri and F. Soavi, Performance Comparison of LMNO Cathodes Produced with Pullulan or PEDOT:PSS Water-Processable Binders, *Energies*, 2022, **15**, 2608.

65 A. Pettignano, A. Charlot and E. Fleury, Solvent-Free synthesis of amidated carboxymethyl cellulose derivatives: Effect on the thermal properties, *Polymers*, 2019, **11**, 1227.

66 A. Manthiram, K. Chemelewski and E.-S. Lee, A perspective on the high-voltage LiMn1.5Ni0.5O4 spinel cathode for lithium-ion batteries, *Energy Environ. Sci.*, 2013, **7**, 1339.

67 C. Julien and M. Massot, Lattice vibrations of materials for lithium rechargeable batteries I. Lithium manganese oxide spinel, *Mater. Sci. Eng., B*, 2003, **97**, 217–230.

68 Y. Wei, K.-B. Kim and G. Chen, Evolution of the local structure and electrochemical properties of spinel LiNi Mn2-O4 (0 x 0.5), *Electrochim. Acta*, 2006, **51**, 3365–3373.

69 H. Dong, Y. Zhang, S. Zhang, P. Tang, X. Xiao, M. Ma, H. Zhang, Y. Yin, D. Wang and S. Yang, Improved High Temperature Performance of a Spinel LiNi0.5Mn1.5O4 Cathode for High-Voltage Lithium-Ion Batteries by Surface Modification of a Flexible Conductive Nanolayer, *ACS Omega*, 2019, **4**, 185–194.

70 G. Oney, J. Serrano-Sevillano, M. Ben-Yahia, J. Olchowka, E. Suard, F. Weill, A. Demortiere, M. Casas-Cabanas, L. Croguennec and D. Carlier, Identification of Degree of Ordering in Spinel LiNi0.5Mn1.5O4 through NMR and Raman Spectroscopies Supported by Theoretical Calculations, *SSRN Electron. J.*, 2024, 6–13.

71 S. H. Oh, K. Y. Chung, S. H. Jeon, C. S. Kim, W. I. Cho and B. W. Cho, Structural and electrochemical investigations on the LiNi0.5-xMn1.5-yMx+yO4 (M = Cr, Al, Zr) compound for 5 V cathode material, *J. Alloys Compd.*, 2009, **469**, 244–250.

72 R. Baddour-Hadjean and J. P. Pereira-Ramos, Raman microspectrometry applied to the study of electrode materials for lithium batteries, *Chem. Rev.*, 2010, **110**, 1278–1319.

73 M. Fehse, N. Etxebarria, L. Otaegui, M. Cabello, S. Martín-Fuentes, M. A. Cabañero, I. Monterrubio, C. F. Elkjær, O. Fabelo, N. A. Enkubari, J. M. L. D. Amo, M. Casas-Cabanas and M. Reynaud, Influence of Transition-Metal Order on the Reaction Mechanism of LNMO Cathode Spinel: An Operando X-ray Absorption Spectroscopy Study, *Chem. Mater.*, 2022, **34**, 6529–6540.

74 J. H. Kim, S. T. Myung, C. S. Yoon, S. G. Kang and Y. K. Sun, Comparative Study of LiNi0.5Mn1.5O 4-d and LiNi0.5Mn1.5O4 Cathodes Having Two Crystallographic Structures: Fd3m and P4332, *Chem. Mater.*, 2004, **16**, 906–914.

75 P. Stüble, V. Mereacre, H. Geßwein and J. R. Binder, On the Composition of LiNi0.5Mn1.5O4 Cathode Active Materials, *Adv. Energy Mater.*, 2023, **13**, 2203778.

76 M. Casas-Cabanas, C. Kim, J. Rodríguez-Carvajal and J. Cabana, Atomic defects during ordering transitions in LiNi0.5Mn1.5O4 and their relationship with electrochemical properties, *J. Mater. Chem. A*, 2016, **4**, 8255–8262.

77 N. E. Asres, N. Etxebarria, I. Monterrubio, D. Saurel, C. F. Elkjær, M. Casas-Cabanas, M. Reynaud, M. Fehse and J. M. L. del Amo, Investigating structural properties and reaction mechanism of non-stoichiometric spinel LNMO via solid state NMR, *J. Mater. Chem. A*, 2023, **11**, 25612–25625.

78 P. Wiechers, A. Hermann, S. Koob, F. Glaum and M. Gleiß, Development of a Process for Direct Recycling of Negative Electrode Scrap from Lithium-Ion Battery Production on a Technical Scale and Its Influence on the Material Quality, *Batteries*, 2024, **10**, 218.